Carbonation of silica cement at high-temperature well conditions

Ruben Bjørge[1], Kamila Gawel[1], Elvia A. Chavez Panduro[2], Malin Torsæter[1]

[1]*SINTEF Industry, 7465 Trondheim, Norway*

[2]*Department of Physics, Norwegian University of Science and Technology, 7491 Trondheim, Norway*

Abstract

Cements for well environments with temperatures above 110°C are typically designed with silica additions. This is the case for many of the wells in the North Sea, which is a region promising for large-scale geological storage of CO_2 from European sources. Wells are probable leakage paths in carbon capture and storage (CCS) projects, and it is therefore important to understand how CO_2 interacts with cement under downhole conditions. In this study, microstructural changes associated with carbonation of cement with and without silica were followed using micro-computed tomography, X-ray diffraction and scanning electron microscopy. The rims of the cement cores exposed to CO_2-saturated brine consisted of a carbonated region and a bicarbonated region. In the silica cement sample, the carbonated region consisted of two distinct layers with a rough interface region containing wormhole-like features. The formation of these two layers in the silica cement is proposed to be due to calcium carbonate dissolution and re-precipitation during exposure to CO_2-saturated brine. The results illustrate the importance of the effect of additives for offshore CO_2-storage well integrity.

Key Words: CO_2 storage; Cement; CO_2 exposure; Well integrity; Silica; CCS

1. Introduction

CCS using depleted oil and gas reservoirs is considered a promising solution for reducing global emissions of greenhouse gases but large-scale implementation is impeded by a fear of CO_2 leakage from the reservoirs (Metz et al., 2005). The special report on CCS published by the Intergovernmental Panel on Climate Change (IPCC) outlines that abandoned and injection wells are among the most probable leakage paths from CO_2 storage sites (Metz et al., 2005). Injection and abandoned wells are man-made structures of several sets of steel pipes (casing) and cement. The risk of CO_2 leakage in these wells comes from different mechanisms, such as cement fracturing, shrinkage or erosion, or casing corrosion (Celia et al., 2005). To avoid leakage, focus on well integrity is important both during injection and as long as the CO_2 is stored ("Well integrity in drilling and well operations, NORSOK D-010," 2013). This implies that CO_2 well integrity has a long-term perspective.

In wells, cement is typically the material used to mechanically support the casing and to provide hydraulic isolation (hinder flow along well annuli, or through the wellbore after well plugging) (Nelson and Guillot, 2006). Unhydrated cement is a complex material containing several compounds, the main mineral being tricalcium silicate, Ca_3SiO_5, abbreviated as C_3S (cement chemist notation) occupying 65% of the volume. Other minerals such as dicalcium silicate (C_2S) and calcium aluminate ferrite (C_4AF) are also present in smaller amounts. When placing cement in wells, it is mixed with water and then pumped into the well. The cement reacts with water forming hydration products. One of the products is calcium silicate hydrate (C-S-H), which is considered the binding element in the cement plug. Calcium hydroxide (CH) also forms filling the pore space in the cement plug. Additionally, non-hydrated particles will be present in cement paste (Nelson and Guillot, 2006).

Silica-based additives like silica flour, fly ash, microsilica, nanosilica, collectively known as pozzolans, can be added to cement when high slurry density, temperature resistivity, mechanical properties, special flow abilities or resistance to acids (Carroll et al., 2016) are required. Such additives have for example been used for high-temperature applications in the North Sea (Bjordal et al., 1993). Similarly, high-temperature geothermal wells require sealing with thermally resistant materials to ensure long-term well integrity (Milestone et al., 2012). Typically, 35%–40% by weight of cement (BWOC) of silica flour is added to prevent *strength retrogression* during hardening at high temperatures (Nelson and Guillot, 2006). When ordinary Portland cement (OPC) hardens at temperatures above 110 °C, the C-S-H phase converts to alpha dicalcium silicate hydrate (α-C_2SH). α-C_2SH is denser than C-S-H, and this transformation is therefore associated with shrinkage and weakening of material strength (Nelson and Guillot, 2006, p. 319). Reducing the lime/silica ratio in the cement, by replacing typically 35–40% of the cement with silica prevents this strength retrogression. With this higher C/S ratio, new phases are formed: tobermorite ($C_5S_6H_5$) at temperatures between 100 and 150°C and xonotlite (C_6S_6H) above 150°C. The presence of these phases does not lead to the loss of mechanical properties or hydraulic sealing ability under normal conditions, i.e., without an acidic environment.

In the presence of CO_2 in an aqueous environment (e.g., CO_2-saturated brine), the cement will react with the CO_2 forming calcium carbonate. The presence of silica-based additives affects this cement carbonation processes. The two phases that form at elevated temperatures, namely tobermorite and xonotlite, are known to have low resistance to carbonation (Nelson and Guillot, 2006 [p.332]). Moreover, the reactions taking place between silica and calcium

hydroxide (CH) during hardening, known as pozzolanic reactions, result in reduced CH content in the cement, which will also affect cement carbonation.

Onan was the first who investigated the effect of CO_2 on cement under well conditions (Onan, 1984). Subsequent studies later investigated the effect of silica content on carbonation of cement at 150°C and 3.5 bar CO_2 (Milestone et al., 1986). They found that high silica content lead to a porous cement that was more prone to attack by CO_2. They therefore found 15 percent silica BWOC to be an optimal balance between strength and calcium hydroxide content at 150°C. Still, current practice is to use 35–40% silica BWOC. Papadakis et al. (1992) also found that pozzolanic cements increases the rate of carbonation due to an increased porosity and reduced formation of calcium carbonate. The increased porosity stems from the lower volume occupied by the products of pozzolanic reactions than those of the hydration reactions. Kutchko et al. (2009) investigated Class H cement with 35/65 and 65/35 pozzolan/cement ratios by volume exposed to CO_2 at 150 bar and 50°C (Kutchko et al., 2009). They found that the carbonation front had moved approximately 4 mm into the 35/65 sample after one week exposure, while it took the carbonation front only two days to reach 5 mm into the 65/35 sample exposed to CO_2-saturated brine. A recent review suggests that pozzolans can enhance cement resistance against CO_2, while calling for further studies (Abid et al., 2015). Another review by Carroll et al. states that the reason for faster carbonation of pozzolan-containing cement is not clear, but that higher porosity and lower content of portlandite is a possible explanation (Carroll et al., 2016). Brandl et al. investigated two different cement systems exposed at 149°C and 207 bar for 1, 3 and 6 months (Brandl et al., 2011): one "conventional" cement system (Portland–G/35%-BWOC-silica-flour) and a pozzolan cement system (Portland-G/silica-flour/pozzolan), with unspecified composition. They found the pozzolan system to be much more resistant to carbonation. They suggested that the increased resistance was due to a carbonation-resistant layer of C-S-H that had formed around some of the pozzolanic particles.

Although the carbonation of neat cement has received a fair amount of attention over the last decades, there is less understanding of the effect of pozzolan-amended cement exposed to CO_2 at temperatures above 110°C. This study addresses this issue by characterizing two different cements (Portland G cement with and without 35% silica flour) before and after exposure to CO_2-saturated brine. Since ordinary Portland cement cannot be used above 110°C, the two cements were heated to different temperatures. This makes quantitative comparisons between behaviour of the two different cements difficult. However, the carbonation sequence in the two different cements were found to be qualitatively different.

2. Methods

2.1 Sample preparation

Two different cements were investigated: ordinary Portland cement, class G (OPC) (*API Spec 10A, Specification for Cements and Materials for Well Cementing*, 2010), and ordinary Portland cement, class G, with 35% silica flour by weight of cement (S35). Compositions and experimental conditions are given in Table 1. The cement and silica flour (mainly in the form of crystalline quartz) were obtained from Norcem Brevik. The cement and silica flour were blended dry before adding to water according to API recommended practice (*API RP 10 B-2, Recommended Practice for Testing Well Cements*, 2013), and poured into a glass beaker. The cement was covered with a layer of mineral oil to prevent evaporation. The beaker was then placed in a pressure cell and kept at 15 bar pressure supplied by nitrogen. The pressure cell was itself kept inside an oven. The S35 cement was cured at 120°C to simulate a high-temperature environment above the strength retrogression limit at 110°C, while OPC was cured at 66°C. S35 was cured for eight weeks to ensure that all of the portlandite had reacted. After curing, smaller samples were cored out from the large cylinders.

2.2 Exposure to CO_2-saturated brine

The cured samples were exposed to CO_2-saturated brine in a pressure cell kept inside a furnace. The OPC and S35 cements were exposed in two separate experiments to avoid possible contamination between samples. In addition, the exposure of the S35 cement was repeated once, with identical outcome, to confirm the results. Before exposure, the samples were kept in a 1 wt percent NaCl saline solution inside an exicator connected to a water aspirator for at least one day. The samples were then transferred to the pressure cell and fresh 1 wt percent NaCl saline solution was added up to approximately 1 cm above the samples. CO_2 was supplied through the top of the cell.

The pressure cell had an internal diameter of 54 mm. The OPC samples, two in number, had diameter of 25 mm and height 25 mm. Three samples of the S35 cement were exposed: two with dimensions Ø15 mm x 20 mm placed on top of a sample with dimensions Ø38 mm x 40 mm. This means that the volume of brine was approximately 3 times the volume occupied by the samples in both exposure experiments. The exposure temperature was 90°C for the OPC samples and 120°C for the S35 samples. The pressure in the cell was 280 bar and the duration of the exposure was 1 week. The pressure was ramped up gradually over 6–8 h. CO_2 was added

manually throughout the experiment to maintain the pressure at 280 bar. At the end of the exposure the pressure and temperature were decreased gradually over 6–8 h.

The pressure and temperature conditions during exposure were different from the conditions during curing, although for the S35 cement the same temperature was used for both curing and exposure. This means that some caution must be taken when relating the results to downhole conditions. However, the effect of the difference in pressure on the exposure of the S35 cement should be small, as previous results indicate that although hydration rate increases with pressure during curing, the effect on the pore structure is negligible (Lin and Meyer, 2009). Similarly, for the OPC cement, we expect the difference in curing and exposure conditions to affect mainly the kinetics, and not the qualitative features of the sample after exposure to CO_2-saturated brine.

2.3 Sample characterization

Permeability of the as-cured cement was measured using a 3.5 wt. percent NaCl solution, with a confining pressure of 150 bar and pore pressure of 50 bar.

X-ray micro-computed tomography (µ-CT) was performed using a Nikon XTH 225 scanner. Polychromatic X-rays from a wolfram anode using an acceleration voltage of 165 kV and an anode current of 160 A was used with an exposure time of 1000 ms per projection image. The number of projections was 1000 and the resolution 26 µm. The three-dimensional volume was obtained using the reconstruction programme CT-Agent. The grayscale values in the images are directly related to the X-ray attenuation within the object. Bright pixels correspond to large X-ray attenuation. The X-ray attenuation coefficient depends on the energy of the X-ray incident beam, the chemical composition and the density of the object. For a given composition, higher density will give more X-ray attenuation. Image visualization and segmentation were carried out using VGstudio (Volume Graphics GmbH) for the 3D representation of the wormhole and AVIZO (Thermo Fisher Scientific) for the 3D representation of the fronts in the sample.

Scanning electron microscopy (SEM) was performed using Hitachi S-3400N and Hitachi SU-6600 scanning electron microscopes. Epoxy was used to stabilize the sample mechanically before cutting and polishing the SEM samples (Kjellsen et al., 2003). The SEM images shown were acquired in the back-scattered electron (BSE) mode. This imaging mode can give atomic-number contrast, with heavier compounds giving a stronger signal.

The relative amounts of crystalline phases in the three distinguished carbonated layers were quantified based on the reference intensity ratio (RIR) semiquantitative method (Hubbard and Snyder, 1988) applied to X-ray diffraction (XRD) patterns measured with corundum as an internal standard. Small amounts of material were carefully scraped off from each layer after cutting the cores in half axially. For each layer, two X-ray powder diffraction patterns were collected in reflection mode on powder spread out on a silicon substrate. The experiments were performed on a Bruker D8 A25 DaVinci X-ray diffractometer with CuK_α radiation (wavelength λ = 1.5418 Å). The diffractograms were collected in the [10°–75°] scattering angle range with a 0.013° step and a total acquisition time of 1 h. The following peaks were used for quantitative RIR analysis: corundum (25.59°), quartz (26.65°), aragonite (26.24°), and vaterite (32.47°). The ratio of the integrated intensitites ($I_{phase}/I_{corundum}$) used for RIR analysis were: 2.08 for quartz, 1.30 for aragonite and 1.01 for vaterite chosen peaks.

3. Results

3.1 As-cured

The permeability of the OPC sample after curing was measured to be 29 nD, while the S35 sample had a permeability of 337 nD.

Figure 1 shows SEM images of the two different samples after curing. The OPC sample has a typical cement microstructure consisting of C-S-H and CH, in addition to unhydrated cement grains (Fig. 1a). SEM of the S35 revealed a homogenous distribution of silica particles, C-S-H, and unhydrated cement grains (Fig. 1b). No CH was observed in SEM. The silica particles had partially been transformed into C-S-H through reactions at the particle surface (Fig. 1c).

XRD measurements confirmed the presence of the minerals observed by SEM (Figure S1). In addition, tobermorite was detected in the S35 sample. No CH was found in this sample, indicating that all the CH had been converted to C-S-H during curing.

3.2 After exposure to CO_2-saturated brine

3.2.1 µ-CT

Figure 2 shows representative cross-sections of a core of each cement sample taken by µ-CT after exposure to CO_2-saturated brine for 1 week. The OPC core had a thin rim (1-3 mm thick) of carbonated cement after exposure. This core had non-carbonated cement in most of the sample interior (L1). In addition to the non-carbonated cement, one layer of carbonated cement (L2) and precipitates on the outside surface of the core (L5) can be distinguished in OPC based

on the tomography images. A narrow, dark dissolution front can also be seen leading (i.e., interior to) the carbonation front.

In the larger S35 core (Ø38 mm), the carbonation front had reached 6-7 mm into the sample. This core, like the OPC sample, has non-carbonated cement in the centre (L1). Three different layers of altered cement (L2-L4) can be distinguished in addition to the outer rim made of precipitate (L5). The interface between the two innermost altered layers (L2/L3) is rough and the difference in the brightness between the two layers indicates a difference in density. The outermost – third – altered layer (L4) is thin and dark, suggesting a low density of the material within this layer. All the layers present within the exposed samples are schematically presented in Figure 2.

The smaller S35 core (Ø15 mm) was completely carbonated throughout the whole volume (Figure S2). Here the layers are somewhat different from the large core. There is a smaller centre region of uniform intensity. Exterior to this centre is a layer with mixed light/dark grey intensity in a sunburst pattern, in some ways similar to the rough L2/L3 interface in the large S35 core. Outside this layer is a more uniform layer similar in appearance to the L3 layer in the large core. The L4 layer is significantly thicker on the smallest core and the layer of the outermost precipitate was thicker compared to the large S35 core as well.

Figure 3a) shows a magnified region of a µ-CT cross section of the large S35 core. The difference in roughness of the two innermost interfaces is clear. Also, small patches near the interface and into the L2 layer are much darker than either the L2 or L3 layers, suggesting that they are pores. A 3D representation of such a dark volume, highligted in Figure 3a), is shown in Figure 3b,c). The pore shows an elongated shape with a very rough surface. The colour scale indicates a density increase towards the walls of the pore, implying that these pores are not empty but filled with weakly absorbing matter, such as pore fluid or amorphous silica.

3.2.2 XRD

Figure 4 shows XRD patterns acquired from the carbonated layers of the samples exposed to CO_2-saturated brine. The carbonated layer of the OPC sample (L2) contained mainly calcium carbonate in the form of aragonite and calcite (Figure 4a).

Figure 4b) shows XRD patterns acquired from the altered layers L2, L3 and L4 of the large diameter S35 core. The three main crystalline phases present in all the three layers were silica in the form of quartz, and two phases of calcium carbonate: vaterite and aragonite. The relative

amounts of crystalline phases in the distinguished altered layers were quantified based on the RIR semiquantitative method applied to XRD patterns measured with corundum as an internal standard (for details see Methods section). As the carbonation process should not significantly influence the crystalline silica it has been assumed that the quartz content is similar in all the layers and the content was set to 1. The content of carbonate phases (aragonite, vaterite) was normalized with respect to quartz content in weight percent. The normalized quantities of aragonite and vaterite for each altered layer in the S35 sample are presented in the Table 2.

The innermost altered layer, L2, was the most abundant in calcium carbonate. L3 contained less calcium carbonate compared to the L2 layer. The most external layer, L4, contained the least calcium carbonate and the total content of it was ten times lower compared to the L2 layer and eight times lower compared to layer L3. The innermost altered layer, L2, contained aragonite but no vaterite, while the more externally located altered layer, L3, was rich in vaterite. The precipitate at the external sample surfaces was calcium carbonate in the phase of aragonite (Figure S3).

3.2.3 SEM

SEM allows us to study the exposed cement sample cross sections with high spatial resolution. Figure 5a) shows a montage of SEM BSE images of the large S35 cylinder shown in Figure 2e-h). The different layers distinguished based on tomography scans (and colour-labeled in Fig. 2) are colour-labeled beneath the image. The unaltered region is visible at the very right. The brightest spots within this layer are unhydrated cement grains. The carbonation front is stretching from top to bottom in the image; it is smooth and straight at this length scale. The next two layers, L2 and L3, were easily distinguishable in the µ-CT cross sections, but this is less so in the SEM images. The L2/L3 interface zone is much more ragged than the smooth carbonation front. What is most striking is the porosity near the transition between these two layers, which appears dark in the SEM images since it is filled with epoxy. These pores were found to be elongated perpendicularly to the carbonation front, as opposed to the pores that were formed during the setting of the cement, which are more spherical. This confirms the observation of pores in the µ-CT images.

The L4 layer close to the surface appears darker, indicating that porosity at this edge is increased. The precipitate region present at the external surfaces is just visible in the leftmost part of the figure.

SEM images of the region near the carbonation front in the OPC and S35 samples are shown in Figure 5b) and c), respectively. The carbonation front in OPC is jagged, while in S35 it is smooth and even. The OPC sample has a wide (200-500 µm) darker region in front of the carbonation front. In the S35 sample this region is almost absent: there is only a very narrow (20-40 µm) strip interior to the carbonation front that is dark.

4. Discussion

4.1 Cement curing

In order to understand the difference in the carbonation processes between OPC and silica cement, the difference in the chemical composition of the two cements (resulting from the differences in the hydration processes) has to be considered. During curing of OPC, a large amount of CH is created. When silica particles are present in the cement, the silica reacts at the surface with CH and forms so called secondary C-S-H. The name "secondary C-S-H" emphasizes that it does not originate from hydration but is a result of pozzolanic reactions between silica and CH which are slower than the initial hydration reactions. The secondary C-S-H is a cementitious compound and is more durable than CH, which may dissolve in water (Nelson and Guillot, 2006). The pozzolanic reactions contribute to increased mechanical strength of silica cement materials and result in lower content of CH in the hardened cement.

The OPC sample contained C-S-H, CH and unreacted cement grains, as expected. The S35 sample did not contain any CH, which means that the curing was long enough for all the CH to react with silica. C-S-H was found at the surface of the quartz grains, presumably due to pozzolanic reactions between the quartz and dissolved CH. The low solubility of quartz in alkaline solution makes it likely that most of the pozzolanic reactions took place at the surface of the quartz, and not through the quartz dissolving and diffusing to the CH. The absence of CH implies that C-S-H was the only solid phase that underwent carbonation during exposure to CO_2-saturated brine.

Interestingly, the permeability of the S35 sample was ten times the permeability of the OPC sample. Silica-amended cement is known to be more porous than OPC. Papadakis et al. ascribe the higher porosity to the higher density of the products of the pozzolanic reactions (mainly C-S-H) compared with the density of silica and CH (Papadakis et al., 1992). Although quartz used in this study is denser than the amorphous silica often present in pozzolans, the pozzolanic C-S-H still has approximately 10 percent lower molar volume than the silica and CH combined (see Table 3 for densities). The relationship between porosity and permeability is not

straightforward, but generally more porosity leads to higher permeability. If the increase in porosity mainly occurred through dissolution of CH and subsequent formation of denser C-S-H at the quartz grain surfaces, one would expect a significant connectivity between the pores, and hence higher permeability. Still, the permeability of both cements after curing was almost three orders of magnitude lower than the API recommendation of 200 µD for a good seal (Kutchko et al., 2009).

4.2 Carbonation

4.2.1 Ordinary Portland cement

The chemical processess involved in the carbonation of ordinary Portland cement in an aqueous environment have been described by Kutchko et. al. (Kutchko et al., 2007):

(1) CO_2 (g) + H_2O <=> H^+ + HCO_3^-

(2) $Ca(OH)_2$ (s) <=> Ca^{2+} + $2OH^-$

(3) Ca^{2+} + $2OH^-$ + H^+ + HCO_3^- <=> $CaCO_3$(s) + $2H_2O$.

First the dissolved CO_2 reacts with water to form carbonic acid (1). When the aqueous solution of carbon dioxide/carbonic acid diffuses into the cement matrix, CH is dissolved (2). This CH dissolution is visible as a darker layer in the tomography cross-section in Fig. 2a) and the SEM image in Fig. 5b) between the unaltered cement and the brighter carbonated cement. The front of this CH-depleted layer has been called the (CH-)dissolution front (Rimmelé et al., 2008).

The carbonic acid can then combine with the dissolved calcium and precipitate in the form of calcium carbonate (3). This process leads to the increase in cement density inside the carbonated layer manifested in the form of higher X-ray attenuation, giving higher brightness in tomography images.

When the pH drops below 11 due to carbonation, the concentration of CO_3^{2-} decreases, and bicarbonate, HCO_3^-, begins to dominate. Now, calcium carbonate is converted to water-soluble calcium bicarbonate (4):

(4) $CaCO_3$(s) + H^+ + HCO_3^- <=> Ca^{2+} + $2HCO_3^-$

The bicarbonation process leads to leaching of cementitious material from the cement matrix. The result is the formation of a porous, layer at the edge of the sample with a significant decrease of the mechanical strength, and low brightness in tomography and SEM images. This stage was not reached in the OPC sample due to the limited time of exposure.

4.2.2 Silica-amended cement

The carbonation front (i.e., the L1/L2 interface) was smoother in the S35 sample than in the OPC sample. Also, the S35 sample had a much narrower region where calcium is dissolved (interior to the L1/L2 interface) prior to carbonation (20-40 µm in S35 vs. 200-500 µm in OPC). This is presumably due to the absence of portlandite in the S35 sample. It is understandable that a wider dissolution region (in the OPC sample) would lead to a less straight carbonation front since one would expect a greater impact of local variations in diffusivity if the calcium ions must diffuse over a longer distance.

Using XRD, the L2 layer was shown to be rich in calcium carbonate in the form of aragonite. That this polymorph of calcium carbonate forms is in line with observations of Wray and Daniels who showed that aragonite is the predominant precipitate at high temperature and pressure from supersaturated solutions of calcium carbonate (Wray and Daniels, 1957). The L3 layer had a slightly lower total calcium carbonate concentration, consisting of vaterite and aragonite in roughly equal amounts. However, there is a difference in intensity between the L2 and L3 layers in the µ-CT images: the L2 is slightly brighter than the L3 layer. Knowing that aragonite has 16 percent higher density than vaterite (see Table 3), we conclude that the contrast between L2 and L3 in the µ-CT images is due to L2 being rich with relatively dense aragonite, and L3 richer in less dense vaterite. That the µ-CT contrast between L2 and L3 is not purely due to a difference in calcium carbonate content is supported by the SEM images in Figure 5a) where there is little difference in intensity between the two layers. The lack of contrast is due to the BSE signal being sensitive to the average atomic number (which is the same for aragonite and vaterite), but insensitive to the mass density as such. The intensity in the µ-CT scan, on the other hand, is dependent on both.

The different polymorphs of calcium carbonate present in L2 and L3 suggests that the interface between the two layers represents an aragonite to vaterite transformation front. According to Weiss et al., at high temperatures vaterite forms at lower pH conditions than aragonite (Weiss et al., 2014). This may suggest that the aragonite formed initially, re-precipitates as vaterite when the pH inside the cement matrix drops to the level favouring vaterite formation. The pores visible in the SEM and µ-CT images of the L2/L3 interface, could be a sign of aragonite dissolution, followed by vaterite precipitation.

The L4 layer is formed after the calcium carbonate is transformed to water-soluble bicarbonate. The bicarbonate dissolves and leaves behind a porous silica gel. The L3/L4 interface does not have the roughness of the L2/L3 interface. Instead, it appears identical to the bicarbonation front in the OPC sample. It is interesting that the L2/L3 and L3/L4 interfaces are

so different despite the transformations presumably having the same driving force, namely the presence of carbonic acid.

The smaller S35 core (Ø15 mm) allows us to study the carbonation process after the carbonation front has reached the centre of the sample. The aragonite-rich L2 and vaterite-rich L3 layers observed in the larger S35 core interpenetrate in the small core. Due to this interpenetration, the XRD results from this region contain a signal from both the bright and dark regions, and hence indicate a mixture of aragonite and vaterite. The bicarbonate layer, L4, is thicker in the smaller S35 core than in the large core, and also the layer of precipitates on the surface is thicker. This difference in thickness is expected since the surface-to-volume of carbonated cement ratio is considerably smaller for the smaller core.

The L1/L2 dissolution/carbonation front and the L3/L4 bicarbonation front are both relatively smooth compared to the quite rough and porous L2/L3 dissolution/re-precipitation front. At the L1/L2 interface, C-S-H dissolves and calcium carbonate (mainly aragonite) forms. At the L2/L3 interface, calcium carbonate dissolves and re-precipitates with a higher amount of vaterite. At the L3/L4 interface, calcium carbonate dissolves, leaving behind an amorphous and porous silica gel.

The L2/L3 front showed a wormhole-like pattern resembling those observed in e.g. acid treatment of carbonate rocks (Gdanski, 1999; Golfier et al., 2002; Ott and Oedai, 2015; Tansey and Balhoff, 2016). However, the L1/L2 and L2/L3 reaction fronts differ from the acid treatment of rocks in that there are two reactions: dissolution and precipitation, instead of only dissolution. Still, the appearance of the fronts depends on the interplay between mass transport of reactants in solution (e.g., Ca^{2+}) and reaction rate (Fredd and Fogler, 1998).

For the acid treatment of carbonate rocks it has been shown that depending on the relative rates of mass transport (advection, convection, diffusion) and reaction several dissolution regimes can be distinguished (Fredd and Fogler, 1998, 1996): (1) At low mass transport rates and high reaction rates acid is quickly and completely consumed at the inlet. Wormhole instabilities cannot develop, and face or compact dissolution is observed. (2) On increasing mass transport rate, instabilities can develop. Acid starts to penetrate the matrix and erodes the walls of the flow channels, leading to the formation of a conical-shaped wormhole. (3) Further increase of the mass transport rates will lead to the formation of dominant wormholes and branched or ramified wormholes due to preferential penetration of acid into the biggest pores/flow channels.

Analogously, one would expect a slow dissolution of C-S-H followed by fast aragonite precipitation to lead to a smooth L1/L2 interface. On the other hand, the presence of wormhole-like pores at the L2/L3 interface may suggest that the dissolution of aragonite is considerably faster than the re-precipitation in the form of vaterite.

5. Conclusions

Microstructural changes associated with carbonation of Portland cement with and without silica were followed using µ-CT, XRD and SEM. Although silica is a common additive to maintain the strength of cements above 110°C, it does not have such an effect when it comes to CO_2 resistance. We observe that the carbonation speed of silica-cement is much higher than that of ordinary Portland cement. When only a thin rim of carbonation is visible for the ordinary Portland cement, the silica-cement sample of similar size is fully carbonated. The difference in carbonation front speed between the OPC and the silica cement might be explained by the difference in cement permeability and exposure temperature. Also, the fact that the silica cement was cured for a longer time than the neat cement may also have affected the difference in carbonation front speed.

The carbonation of the OPC sample followed three steps: dissolution of portlandite, precipitation of calcium carbonate, and finally formation of soluble bicarbonate, as previously described in the literature. The silica cement differed in exhibiting an irregular transition region with wormhole-like features, within the carbonated region. Semiquantitative XRD showed that this interface separated the carbonated region into an aragonite-rich layer and a mixed aragonite/vaterite layer. We suggested that this transformation could be driven by a change in the local concentration of ions (including pH) as carbonation proceeds.

Further investigations might, for example, consider the effect of the type of pozzolan on the effect of exposure to CO_2. *In-situ* X-ray tomography of CO_2 exposure at high-pressure, high-temperature conditions would also be helpful (Chavez Panduro et al., 2017).

Acknowledgement

Dag W. Breiby is gratefully acknowledged for helpful comments and suggestions in preparing this manuscript. This publication has been produced in the projects "Closing the gaps in CO_2 well plugging" and "Ensuring well integrity during CO_2 injection" funded by the Research

Council of Norway's CLIMIT programme (243765/E20, 233893/E20). The projects are administered as an integrated part of the BIGCCS Centre funded by Gassco, Shell, Statoil, Total, Engie and the Research Council of Norway (193816/S60).

References

Abid, K., Gholami, R., Choate, P., Nagaratnam, B.H., 2015. A review on cement degradation under CO2-rich environment of sequestration projects. J. Nat. Gas Sci. Eng. 27, 1149–1157. https://doi.org/10.1016/j.jngse.2015.09.061

Allen, A.J., Thomas, J.J., Jennings, H.M., 2007. Composition and density of nanoscale calcium-silicate-hydrate in cement. Nat. Mater. 6, 311–316. https://doi.org/10.1038/nmat1871

Anthony, J.W., Bideaux, R.A., Bladh, K.W., Nichols, M.C. (Eds.), 2003. Handbook of Mineralogy. Mineralogical Society of America.

API RP 10 B-2, Recommended Practice for Testing Well Cements, 2nd ed, 2013. . API, Washington, DC.

API Spec 10A, Specification for Cements and Materials for Well Cementing, 24th ed, 2010. . API, Washington, DC.

Bjordal, A., Harris, K.L., Olaussen, S.R., 1993. Colloidal Silica Cement: Description and Use in North Sea Operations, in: Offshore Europe. Society of Petroleum Engineers, pp. 431–440. https://doi.org/10.2118/26725-MS

Brandl, A., Cutler, J., Seholm, A., Sansil, M., Braun, G., 2011. Cementing Solutions for Corrosive Well Environments. SPE Drill. Complet. 26, 208–219. https://doi.org/10.2118/132228-PA

Carroll, S., Carey, J.W., Dzombak, D., Huerta, N.J., Li, L., Richard, T., Um, W., Walsh, S.D.C., Zhang, L., 2016. Review: Role of chemistry, mechanics, and transport on well integrity in CO2 storage environments. Int. J. Greenh. Gas Control 49, 149–160. https://doi.org/10.1016/j.ijggc.2016.01.010

Celia, M.A., Bachu, S., Nordbotten, J.M., Gasda, S.E., Dahle, H.K., 2005. Quantitative estimation of CO2 leakage from geological storage: Analytical models, numerical models, and data needs, in: Greenhouse Gas Control Technologies 7. pp. 663–671. https://doi.org/10.1016/B978-008044704-9/50067-7

Chavez Panduro, E.A., Torsæter, M., Gawel, K., Bjørge, R., Gibaud, A., Yang, Y., Bruns, S., Zheng, Y.,

Sørensen, H.O., Breiby, D.W., 2017. In-Situ X-ray Tomography Study of Cement Exposed to CO_2 Saturated Brine. Environ. Sci. Technol. 51, 9344–9351. https://doi.org/10.1021/acs.est.6b06534

Fredd, C.N., Fogler, H.S., 1998. Influence of transport and reaction on wormhole formation in porous media. AIChE J. 44, 1933–1949. https://doi.org/10.1002/aic.690440902

Fredd, C.N., Fogler, H.S., 1996. Alternative Stimulation Fluids and Their Impact on Carbonate Acidizing, in: SPE Formation Damage Control Symposium. Society of Petroleum Engineers. https://doi.org/10.2118/31074-MS

Gdanski, R., 1999. A Fundamentally New Model of Acid Wormholing in Carbonates 54719–MS. https://doi.org/10.2118/54719-MS

Golfier, F., Zarcone, C., Bazin, B., Lenormand, R., Lasseux, D., Quintard, M., 2002. On the ability of a Darcy-scale model to capture wormhole formation during the dissolution of a porous medium. J. Fluid Mech. 457, 213–254. https://doi.org/10.1017/S0022112002007735

Haynes, W.M. (Ed.), 2011. CRC Handbook of Chemistry and Physics, 92nd ed. CRC Press, Boca Raton, FL.

Hubbard, C.R., Snyder, R.L., 1988. RIR — Measurement and Use in Quantitative XRD. Powder Diffr. 3, 74–77. https://doi.org/10.1017/S0885715600013257

Kjellsen, K.O., Monsøy, a., Isachsen, K., Detwiler, R.J., 2003. Preparation of flat-polished specimens for SEM-backscattered electron imaging and X-ray microanalysis - Importance of epoxy impregnation. Cem. Concr. Res. 33, 611–616. https://doi.org/10.1016/S0008-8846(02)01029-3

Kutchko, B.G., Strazisar, B.R., Dzombak, D. a., Lowry, G. V., Thauiow, N., 2007. Degradation of well cement by CO2 under geologic sequestration conditions. Environ. Sci. Technol. 41, 4787–4792. https://doi.org/10.1021/es062828c

Kutchko, B.G., Strazisar, B.R., Huerta, N., Lowry, G. V., Dzombak, D.A., Thaulow, N., 2009. CO2 reaction with hydrated class H well cement under geologic sequestration conditions: Effects of flyash admixtures. Environ. Sci. Technol. 43, 3947–3952. https://doi.org/10.1021/es803007e

Lin, F., Meyer, C., 2009. Hydration kinetics modeling of Portland cement considering the effects of curing temperature and applied pressure. Cem. Concr. Res. 39, 255–265. https://doi.org/10.1016/j.cemconres.2009.01.014

Milestone, N.B., Bigley, C.H., Durant, A.T., Sharp, M.D.W., 2012. Effects of CO2 on Geothermal Cements. Geotherm. Resour. Counc. Trans. 36, 6.

Milestone, N.B., Sugama, T., Kukacka, L.E., Carciello, N., 1986. Carbonation of Geothermal Grouts - Part 1: CO2 Attack at 150C. Cem. Concr. Res. 16, 941–950.

Nelson, E.B., Guillot, D. (Eds.), 2006. Well Cementing, 2nd ed. Schlumberger. https://doi.org/10.1017/CBO9781107415324.004

Onan, D.D., 1984. Effects of Supercritical Carbon Dioxide on Well Cements. Soc. Pet. Eng. AIME, SPE 161–172.

Ott, H., Oedai, S., 2015. Wormhole formation and compact dissolution in single- and two-phase CO2-brine injections. Geophys. Res. Lett. 42, 2270–2276. https://doi.org/10.1002/2015GL063582

Papadakis, V.G., Fardis, M.N., Vayenas, C.G., 1992. Hydration and carbonation of pozzolanic cements. ACI Mater. J. 89, 119–130.

Richardson, I.G., 2008. The calcium silicate hydrates. Cem. Concr. Res. 38, 137–158. https://doi.org/10.1016/j.cemconres.2007.11.005

Rimmelé, G., Barlet-Gouédard, V., Porcherie, O., Goffé, B., Brunet, F., 2008. Heterogeneous porosity distribution in Portland cement exposed to CO2-rich fluids. Cem. Concr. Res. 38, 1038–1048. https://doi.org/10.1016/j.cemconres.2008.03.022

Tansey, J., Balhoff, M.T., 2016. Pore Network Modeling of Reactive Transport and Dissolution in Porous Media. Transp. Porous Media 113, 303–327. https://doi.org/10.1007/s11242-016-0695-x

Weiss, C. a, Torres-Cancel, K., Moser, R.D., Allison, P.G., Gore, E.R., Chandler, M.Q., Malone, P.G., 2014. Influence of Temperature on Calcium Carbonate Polymorph formed from Ammonium Carbonate and Calcium Acetate. J. Nanotechnol. Smart Mater. 1, 1–6.

Well integrity in drilling and well operations, NORSOK D-010, 2013.

Wray, J.L., Daniels, F., 1957. Precipitation of Calcite and Aragonite. J. Am. Chem. Soc. 79, 2031–2034. https://doi.org/10.1021/ja01566a001

Tables

Table 1. Overview of cement samples investigated.

Sample name	**OPC**	**S35**
Silica content (BWOC)	0 %	35 %

Silica [g]	0	205
Cement [g]	792	587
Water [g]	349	349
Water/solids	0.44	0.44
Curing conditions	66°C / 15 bar / 1 week	120° / 15 bar / 8 weeks
CO_2 exposure	90°C / 280 bar / 1 week	120°C / 280 bar / 1 week

497

498 **Table 2.** Content of carbonate phases, by weight, with respect to crystalline silica (quartz), as
499 determined by the RIR semiquantitative method.

Layer	**L2**	**L3**	**L4**
Silica	**1**	**1**	**1**
Aragonite	**3**	**1.1**	**0.1**
Vaterite	**0**	**1.4**	**0.2**
Total $CaCO_3$	**3**	**2.5**	**0.3**

500 **Table 3**. Density of various phases.

Phase	**Density**	**Reference**
C-S-H ($C_{1.7}SH_{1.8}$)	2.604	(Allen et al., 2007)
Portlandite	2.23	(Anthony et al., 2003)
α-C_2SH	2.721	(Richardson, 2008)
Quartz	2.65	(Anthony et al., 2003)
Amorphous silica	2.196	(Haynes, 2011)
Calcite	2.71	(Anthony et al., 2003)
Aragonite	2.95	(Anthony et al., 2003)
Vaterite	2.54	(Anthony et al., 2003)

501

502

503 **Figures**

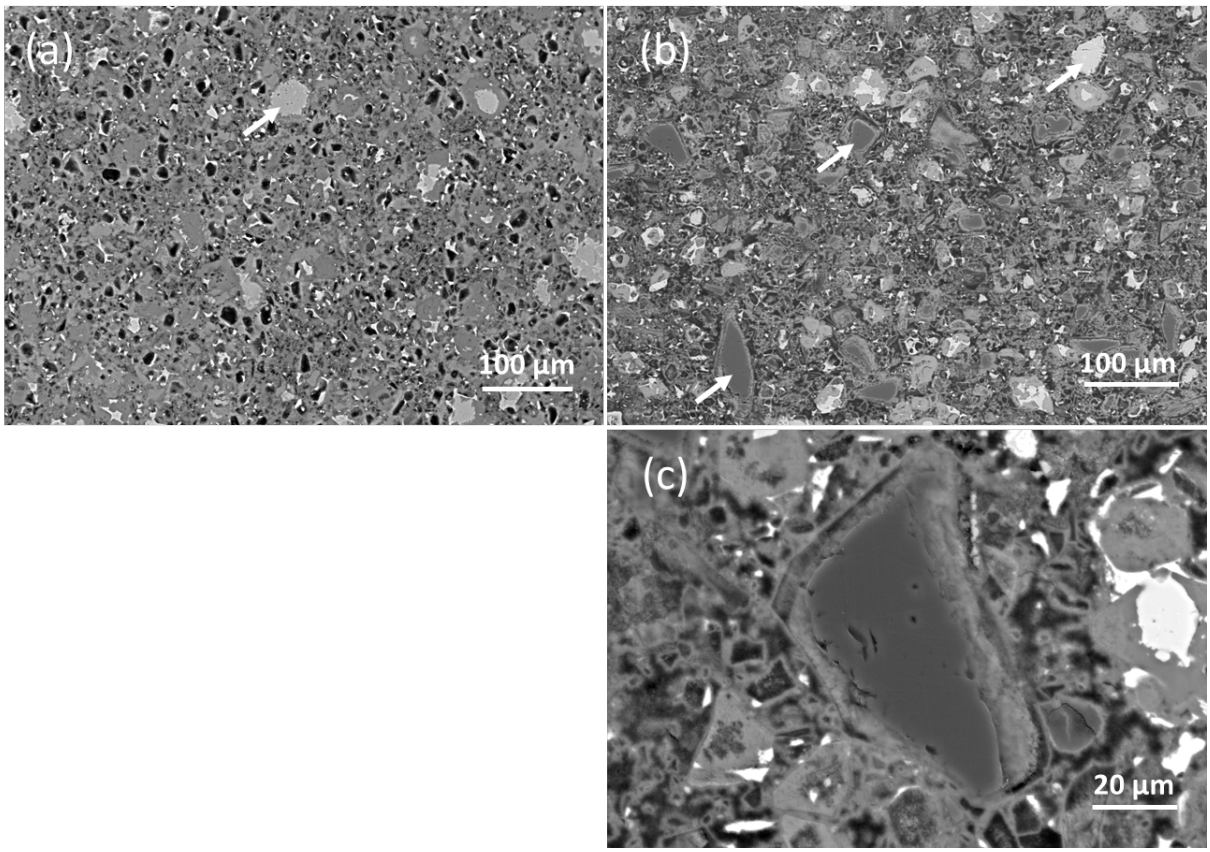

Fig. 1 BSE SEM images of as-cured cement. (a) OPC sample. One cluster of unhydrated cement grains is indicated by an arrow. (b) S35 sample. One group of unhydrated cement grains is indicated by an arrow in the top-right corner. Two silica grains are also pointed to by arrows. (c) Closer view of a silica grain in the S35 sample. The edge of the silica grain has been consumed in pozzolanic reactions, forming C-S-H.

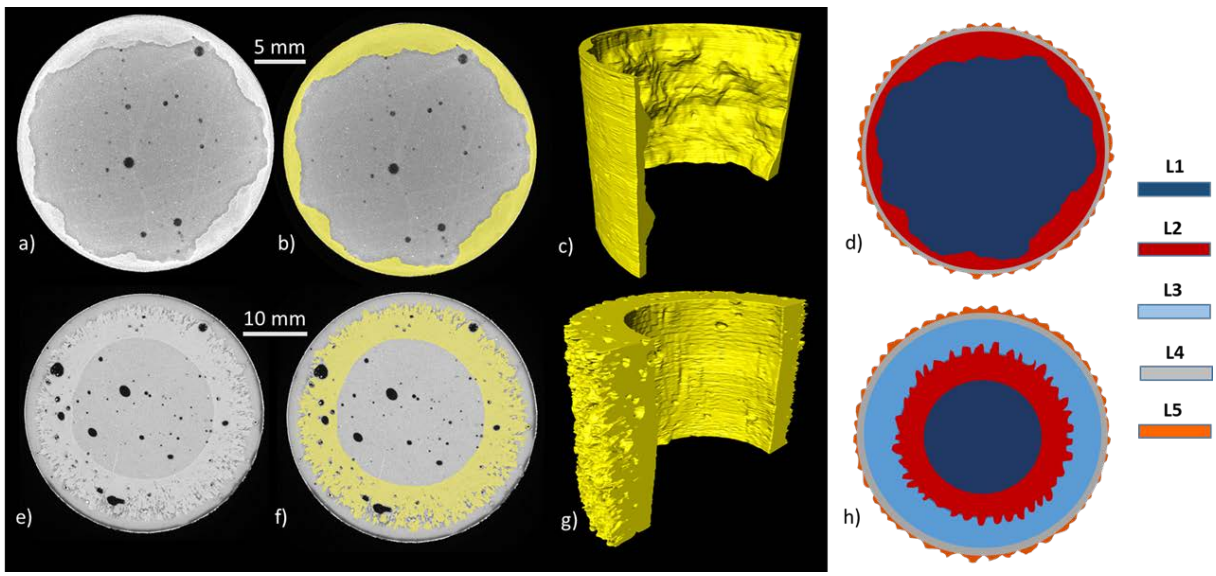

Fig. 2. X-ray computed tomography cross-sections through a) 25 mm OPC core and e) 38 mm S35 core exposed for one week to CO_2-saturated brine. The carbonated layer in OPC and the innermost

carbonated layer in S35 are highlighted in yellow in b) and f), respectively. 3D representation of the carbonated layers c) and g). Schematic representation of different layers observed within the OPC core d), and the large S35 core h).

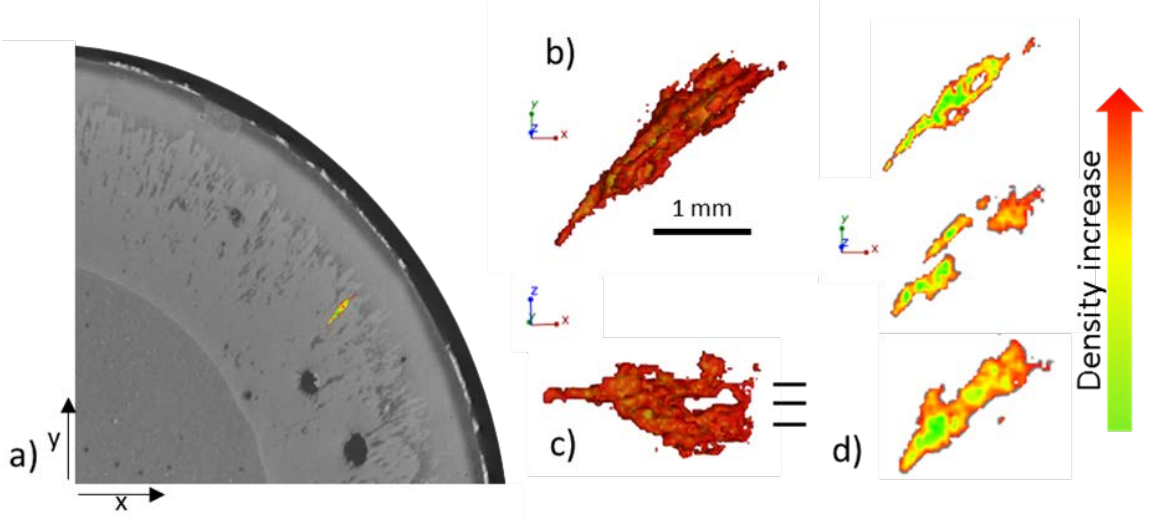

Fig. 3. a) µ-CT cross section of the large (Ø38 mm) S35 core showing location of the chosen pore. b) and c) 3D µ-CT images of the pore from two different views. d) Cross sections of the pore. Black lines in c) indicate the position of the sections. The density increases towards the walls of the pore.

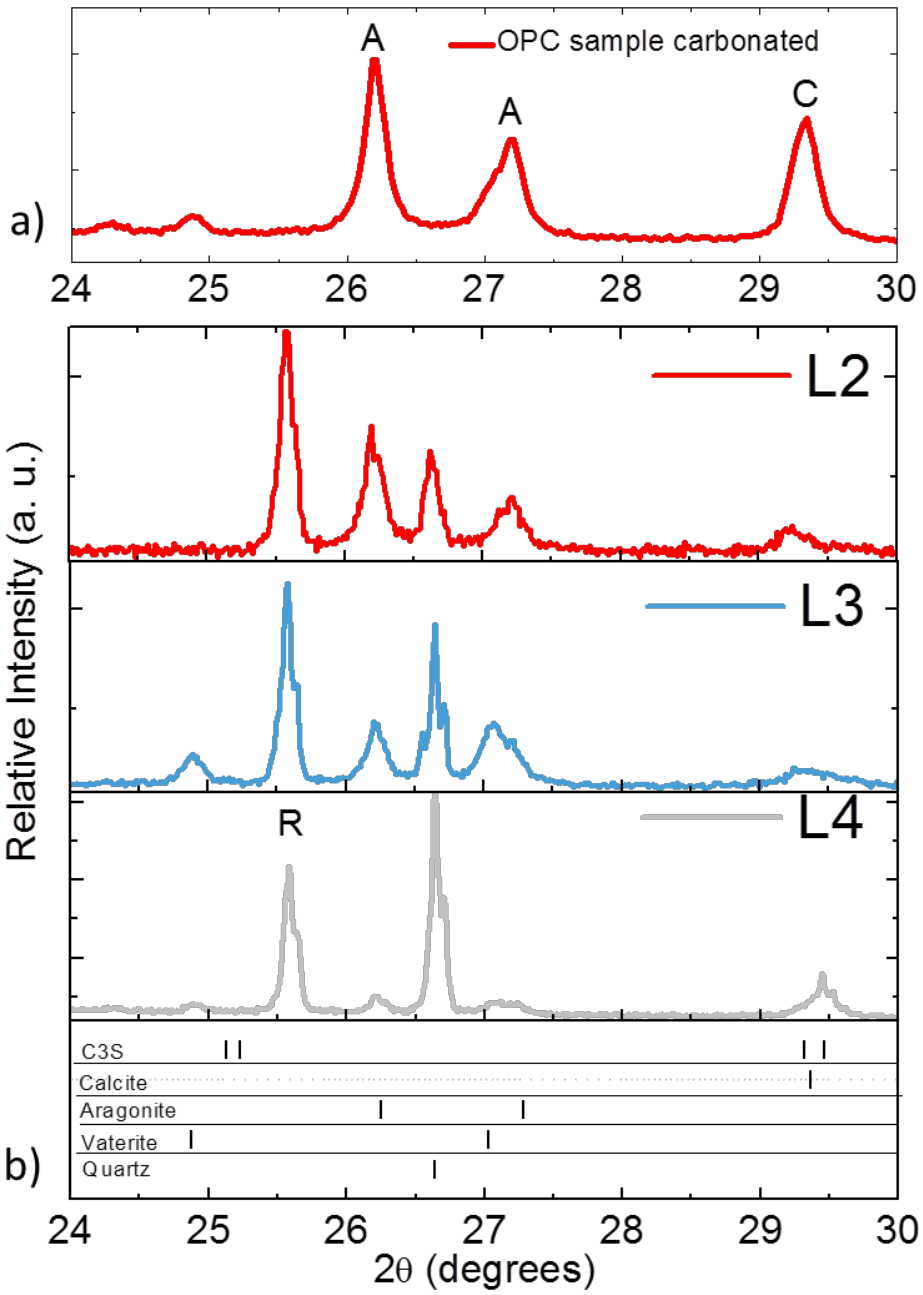

521

522 **Fig. 4.** X-ray diffraction patterns taken from a) carbonated layer (L2) of the OPC core and b) the layers
523 L2, L3 and L4 of the large S35 core (Ø38 mm). Bragg reflections of calcite (PDF 04-012-0489), vaterite
524 (PDF 04-015-9018), aragonite (PDF 00-041-1475), C_3S (PDF 00-055-0739) and quartz (PDF 00-046-
525 1045) are indicated by vertical markers. The peak of the internal standard (corundum) is labelled R.

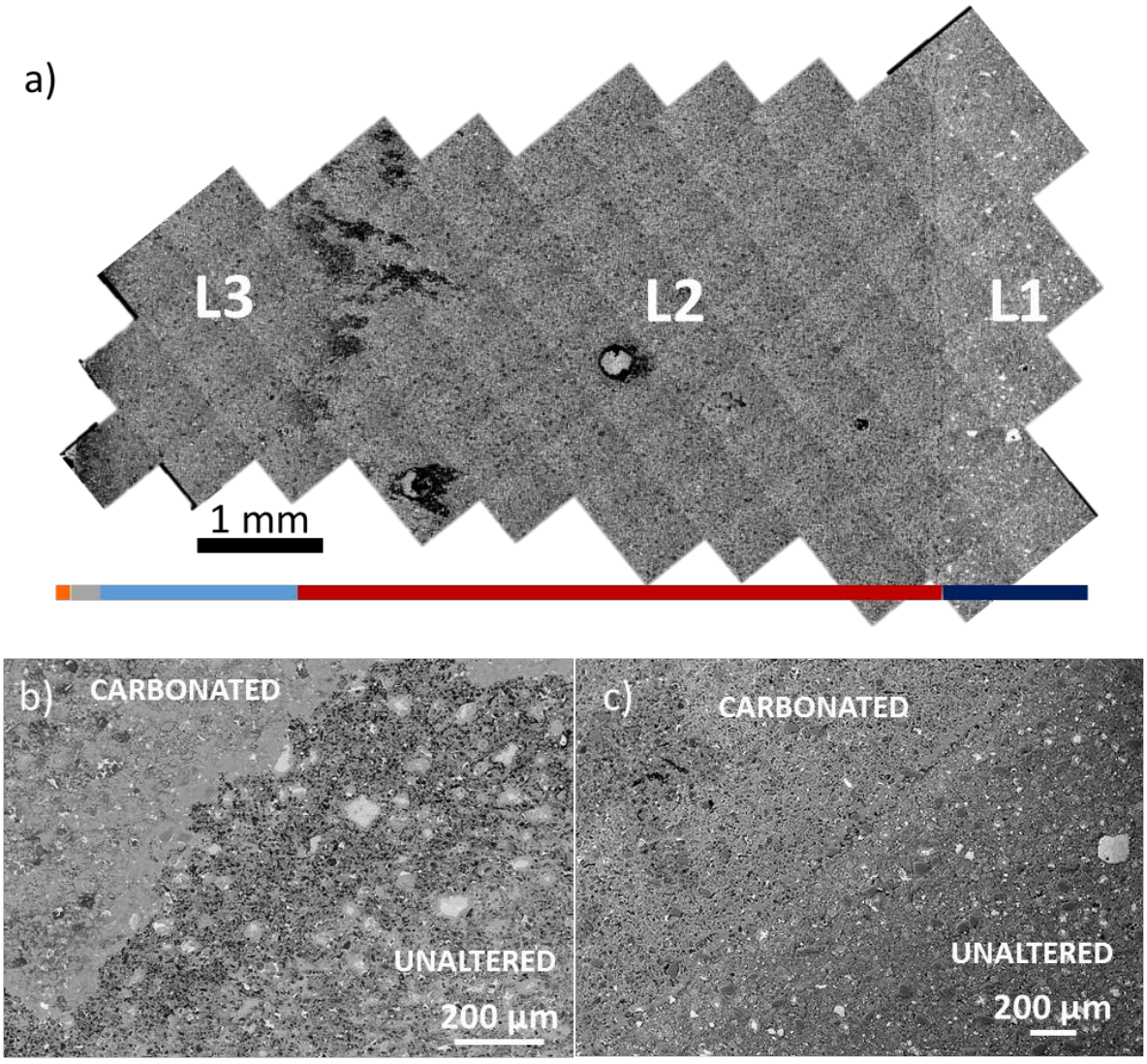

Fig. 5. SEM images of the exposed samples. (a) Montage of images of the large (Ø38 mm) core of the carbonated silica cement sample. The colour-coded bar indicates the location of the different layers distinguished based on CT scans (see Figs. 2 and 3). (b) Region near the carbonation front of OPC sample. The dissolution region between the carbonated and unaltered regions is 200-500 µm wide. (c) Same for S35 sample. The dissolution region is much narrower, and the carbonation front straighter than in the OPC sample.